Electronic Supplementary Information for Optimizing kesterite solar cells from Cu_2ZnSnS_4 to $Cu_2CdGe(S,Se)_4$

Robert B. Wexler†, Gopalakrishnan Sai Gautam†, and Emily A. Carter†‡

†Department of Mechanical and Aerospace Engineering, Princeton University, Princeton, NJ 08544-5263, United States and ‡ Office of the Chancellor and Department of Chemical and Biomolecular Engineering, University of California, Los Angeles, CA 90095, United States

S1. Effect of Mg- and Si-substitution on CZTS

Table S1. DFT-SCAN 0 K formation energies (ΔE_f^{0K}) and experimental 298 K formation enthalpies (ΔH_f^{298K}) of MgS and SiS_2, which are in equilibrium with Cu_2MgSnS_4 (CMTS)[1] and Cu_2ZnSiS_4 (CZSiS), respectively, under Cu-poor conditions.

Compound	ΔE_f^{0K} (eV)	ΔH_f^{298K} (eV)[2]
MgS ($Fm\bar{3}m$, 225)[3]	-3.33	-3.64
SiS_2 ($Ibam$, 72)[4]	-2.26	-2.21

Table S2. DFT-SCAN chemical potentials (μ) for Cu-poor Cu-Mg-Sn-S and Cu-Zn-Si-S equilibria. The μ are referenced to the DFT-SCAN energies of the pure elements in their DFT-SCAN-optimized ground-state structures at 0 K, i.e., $Fm\bar{3}m$ (225) for Cu,[5] $P6_3/mmc$ (194) for Zn[6] and Mg[7], $Fd\bar{3}m$ (227) for Sn[8] and Si,[9] and $FdddZ$ (70) for S.[10]

Compounds in equilibrium	μ (eV/atom)					
	Cu	Zn	Mg	Sn	Si	S
CMTS-MgS-SnS_2-S	-0.49	n/a	-3.33	-1.27	n/a	0
CZSiS-ZnS-SiS_2-S	-0.59	-1.88	n/a	n/a	-2.26	0

Table S3. DFT-SCAN defect formation energies (ΔE_f^d) for CMTS and CZSiS under Cu-poor conditions (see Table S2). CZTS is included for comparison. Relative to CZTS, complete Mg-substitution promotes the formation of detrimental defects (Cu_{Mg}+Mg_{Cu} decreases the V_{oc} and $2Cu_{Mg}$+Sn_{Mg} decreases the I_{sc}) and suppresses the formation of the beneficial V_{Cu}, which increases the V_{oc}. Complete Si-substitution, on the other hand, has the opposite effect, i.e., it suppresses Cu_{Zn}+Zn_{Cu} and $2Cu_{Zn}$+Si_{Zn} and promotes V_{Cu}. Unfortunately, the band gap of CZSiS is too large (2.97-3.07 eV[11] vs. $E_g^{SQ} = 1.34$ eV), thus precluding it from further consideration.

Defect	ΔE_f^d (eV)		
	CMTS (X=Mg and Y=Sn)	CZSiS (X=Zn and Y=Si)	CZTS (X=Zn and Y=Sn)
Cu_X+X_{Cu}	0.11	0.26	0.22
V_{Cu}	0.30	0.05	0.17
$2Cu_X$+Y_X	-0.01	1.17	0.67

S2. Stability of CCdGSSe Against Phase Separation and Decomposition

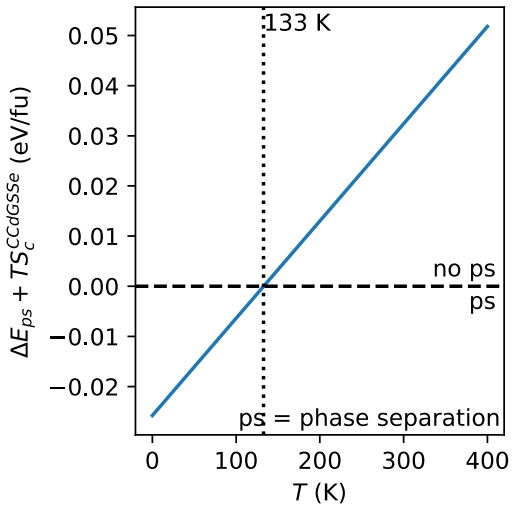

Figure S1. Thermodynamics of Cu_2CdGeS_3Se phase separation (ps), i.e., Cu_2CdGeS_3Se → ¾ Cu_2CdGeS_4 + ¼ $Cu_2CdGeSe_4$. ΔE_{ps} is the DFT-SCAN total energy change of phase separation in eV per formula unit (fu), T is the temperature in K, and S_c is the configurational entropy, which for CCdGSSe is the mixing entropy of an ideal solid-solution of S and Se on the anion sublattice. S_c stabilizes CCdGSSe for $T \geq 133$ K against phase separation. We have $+TS_c$ rather than $-TS_c$ on the vertical axis because only the reactant CCdGSSe has configurational degrees of freedom.

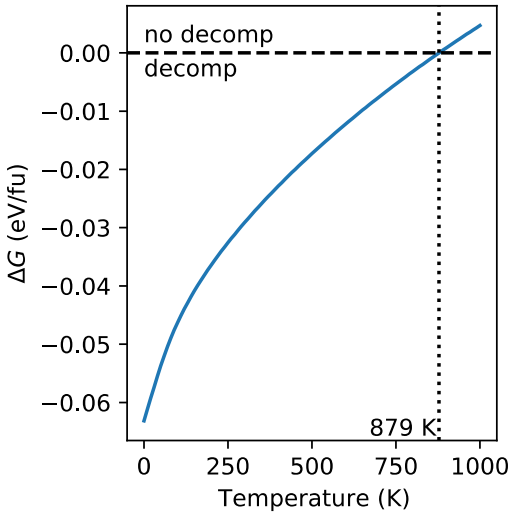

Figure S2. Temperature (T) dependence of the change in free energy (ΔG) upon CCdGSSe decomposition (decomp) into Cu_2GeS_3 and CdSe, i.e., Cu_2CdGeS_3Se → Cu_2GeS_3 + CdSe. $\Delta G = \Delta E + \Delta F_v + TS_c$ where ΔE is the change in the DFT-SCAN total energy (E), ΔF_v is the change in vibrational (v) free energy calculated from the phonon density of states (DOS) under the harmonic approximation (see Figure S3 and Table S4 for the phonon DOS and standard entropies, respectively), and S_c is the configurational (c) entropy, which for CCdGSSe is the mixing entropy of an

ideal solid-solution of S and Se on the anion sublattice. $\Delta F_v + TS_c$ stabilizes CCdGSSe for $T \geq 879$ K. We have $+TS_c$ rather than $-TS_c$ in the ΔG expression because only the reactant CCdGSSe has configurational degrees of freedom.

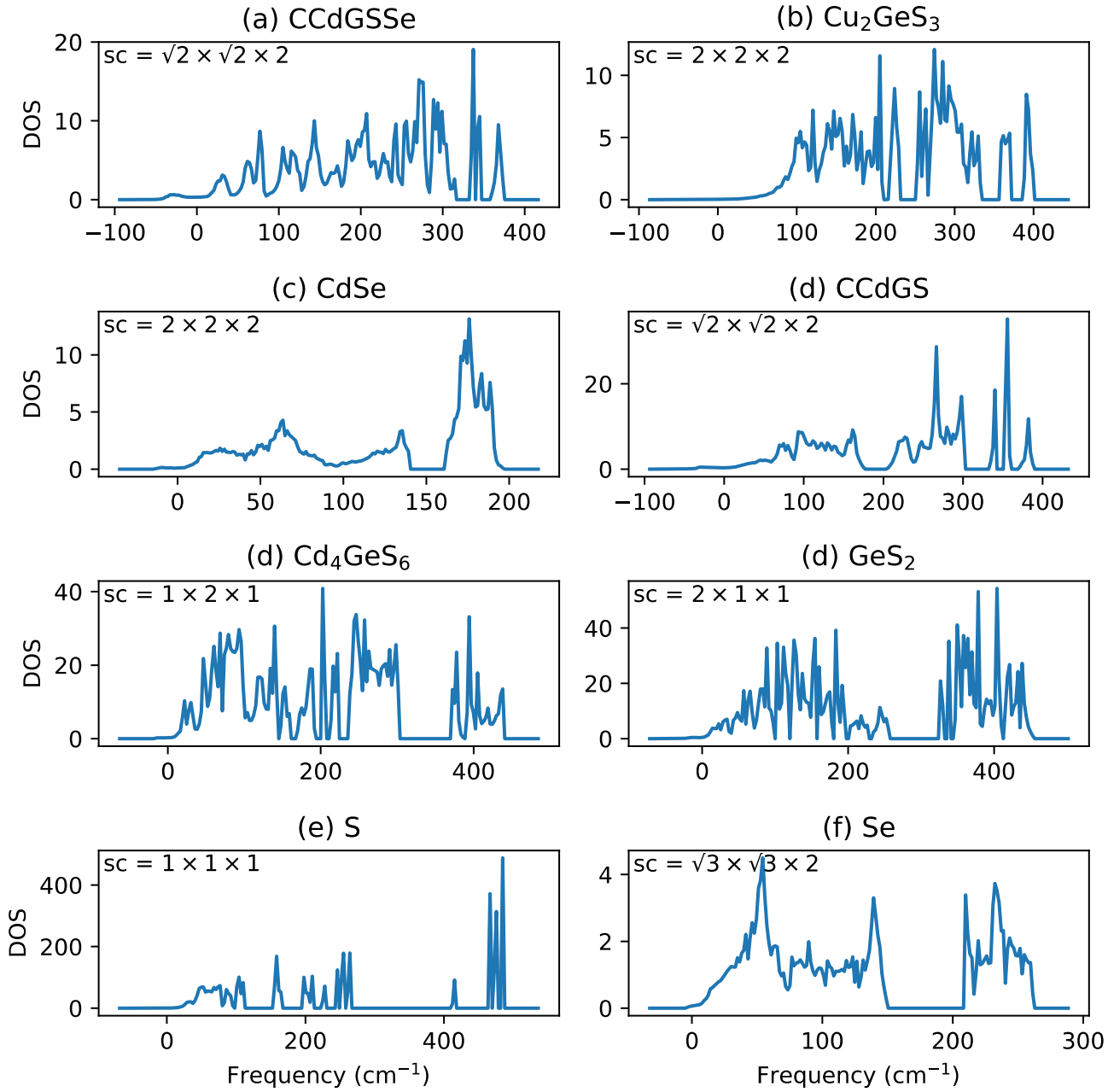

Figure S3. Phonon density of states (DOS) under the harmonic approximation for CCdGSSe, its decomposition products (Cu_2GeS_3 and CdSe), and the compounds in equilibrium under Cu-poor conditions (CCdGS, Cd_4GeS_6, GeS_2, S, and Se). We used a √2×√2×2 supercell (sc) for (a) CCdGSSe and (d) CCdGS because they adopt a subtle √2×√2 tetrahedral tilting pattern along the a and b lattice vectors. We calculated the phonon DOS from finite central differences (displacement amplitude is 0.01 Å) on an 8×8×8 Monkhorst-Pack mesh, as implemented in phonopy.[25]

We used a convergence threshold of 1×10^{-8} eV for SCF loops. Additionally, we evaluated the PAW projectors in reciprocal space and used an additional support grid for the evaluation of the PAW-DFT augmentation charges.

Table S4. Agreement between DFT-SCAN and experimental (including uncertainties) standard entropies. DFT-SCAN corresponds to vibrational entropies calculated from the phonon density of states under the harmonic approximation.

Material	Entropy at 298 K and 1 bar (J/mol/K)			Reference
	DFT-SCAN	Experimental	Uncertainty	
CCdGSSe	227.56	n/a	n/a	n/a
Cu_2GeS_3	154.84	190.3	5.5	26
CdSe	84.97	83.26	2.09	2
CCdGS	231.19	n/a	n/a	n/a
Cd_4GeS_6	363.24	n/a	n/a	n/a
GeS_2	84.32	87.45	2.09	2
S	29.64	32.97	0.42	2
Se	43.00	42.26	0.42	2

S3. Lowest Energy Ionic Configurations for Bulk Structures

S3.1. Ge-substituted CZTS

S3.1.1. ↓CZTGS

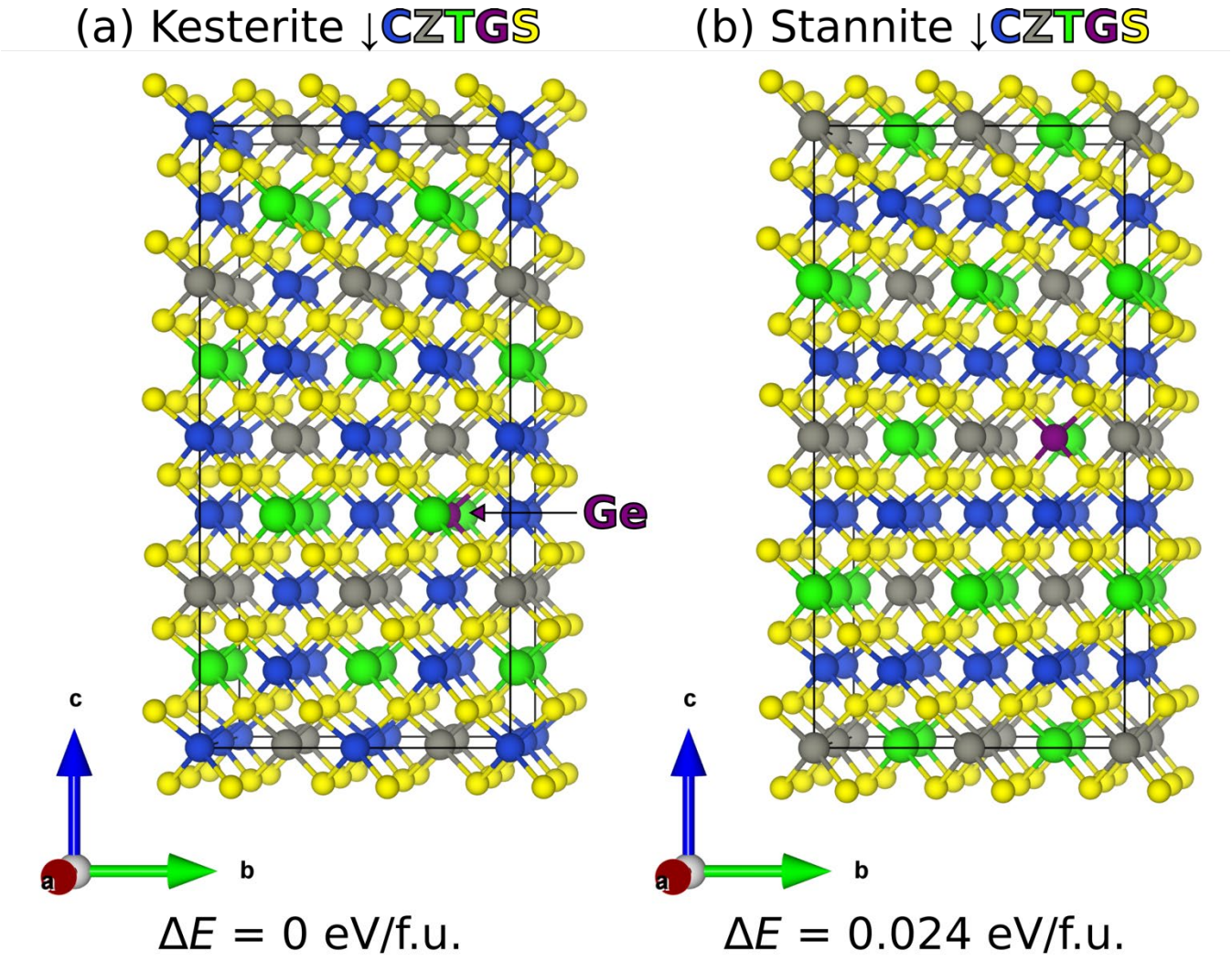

Figure S4. Ionic configuration of (a) kesterite and (b) stannite ↓CZTGS. Stannite is 0.024 eV/f.u. less stable than kesterite (see light blue bar in **Figure 4a** in the main text). Blue, gray, green, purple, and yellow balls correspond to Cu, Zn, Sn, Ge, and S, respectively (see multicolor labels). VASP POSCAR files containing the total energies, lattice geometries, and ionic positions of these structures can be found in "Structures/S3.1.1/".

S3.1.2. ↑CZTGS

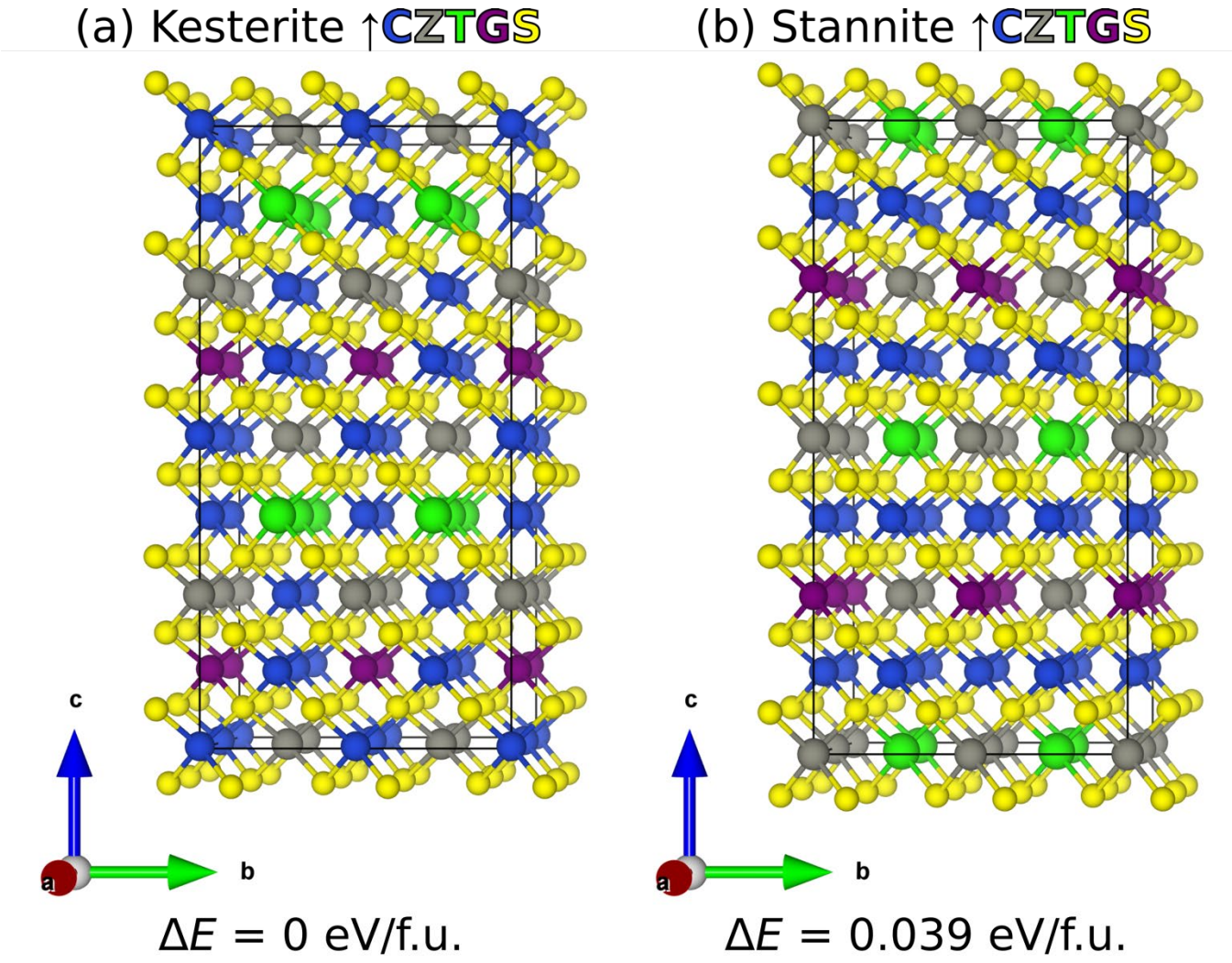

Figure S5. Ionic configuration of (a) kesterite and (b) stannite ↑CZTGS. Stannite is 0.039 eV/f.u. less stable than kesterite (see dark blue bar in **Figure 4a** in the main text). Blue, gray, green, purple, and yellow balls correspond to Cu, Zn, Sn, Ge, and S, respectively (see multicolor labels). VASP POSCAR files containing the total energies, lattice geometries, and ionic positions of these structures can be found in "Structures/S3.1.2/".

S3.2. Se-substituted CZGS

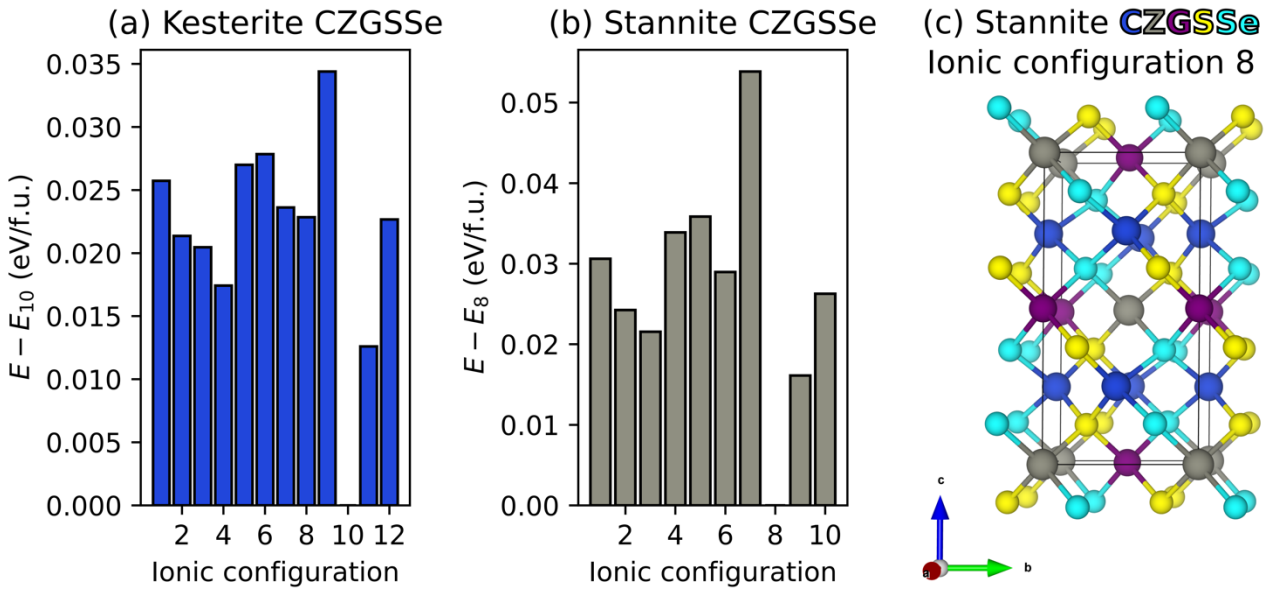

Figure S6. Relative energies of all symmetry-unique S/Se configurations in the 16-atom conventional cell of (a) kesterite and (b) stannite $Cu_2ZnGeS_2Se_2$ (CZGSSe). For kesterite, energies are relative to ionic configuration 10, which is shown in **Figure 5a** of the main text. For stannite, energies are relative to ionic configuration 8 (panel c), which has the same S/Se configuration as the lowest-energy kesterite configuration. Blue, gray, purple, yellow, and cyan balls correspond to Cu, Zn, Ge, S, and Se, respectively (see multicolor labels). VASP POSCAR files containing the total energies, lattice geometries, and ionic positions of these structures can be found in "Structures/S3.2/".

S3.3. Cd- and Se-substituted CZGS

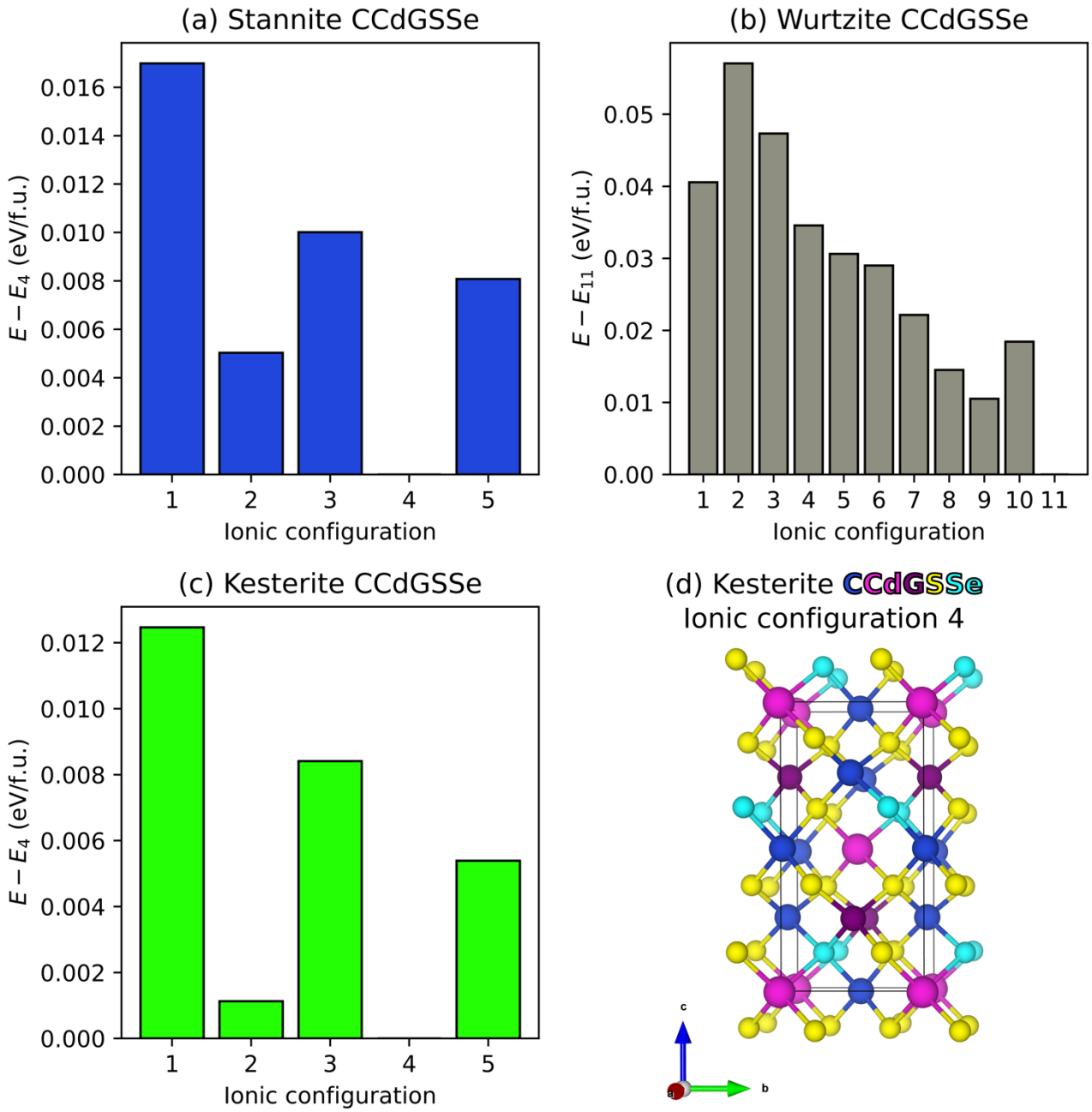

Figure S7. Relative energies of all symmetry-unique S/Se configurations in the 16-atom conventional cell of (a) stannite, (b) wurtzite, and (c) kesterite Cu_2CdGeS_3Se (CCdGSSe). For stannite (wurtzite), energies are relative to ionic configuration 4 (11), which is shown **in Figure 6a** (**6b**) of the main text. For kesterite, energies are relative to ionic configuration 4 (panel d). Blue, magenta, purple, yellow, and cyan balls correspond to Cu, Cd, Ge, S, and Se, respectively (see multicolor labels). VASP POSCAR files containing the total energies, lattice geometries, and ionic positions of these structures can be found in "Structures/S3.3/".

S4. Polymorph Stability for Quaternary Chalcogenides Containing Zn

Table S5. Energies of the stannite and wurtzite polymorphs for CZTS, CZGS, $Cu_2ZnSnSe_4$ (CZTSe), and $Cu_2ZnGeSe_4$ (CZGSe) relative to their ground state kesterite phases. We did not include wurtzite in Figures 4a and 5c in the main text because it is less stable than both kesterite and stannite for all four Zn-containing quaternary chalcogenides we considered and therefore is not experimentally relevant.

Composition	$E - E_{kesterite}$ (eV/f.u.)	
	Stannite	Wurtzite
CZTS	0.028	0.068
CZGS	0.041	0.048
CZTSe	0.030	0.089
CZGSe	0.047	0.074

S5. Defect Generation Protocol

Table S6. Protocol used to generate defects in $2 \times 2 \times 2$ supercells of their defect-free, bulk kesterite, stannite, or wurtzite structures. X is Zn, Cd, or Mg; Y is Sn, Ge, or Si. Exceptions: (1) for Cu_X+X_{Cu} in CZGSe, CMTS, and CZSiS, we considered only the configuration where Cu_X and X_{Cu} form adjacently in the same, Zn-containing (001) plane, as this is the lowest-energy configuration for CZTS, CZTGS, CZGS, and CZGSSe; (2) for $Cu_{Cd}+Cd_{Cu}$ in wurtzite CCdGSSe, we increased the threshold distance from 4.5 Å to 5 Å; (3) for $2Cu_X+Y_X$ in CZGSe, CMTS, and CZSiS, we considered only the configuration where the $2Cu_X$ and Y_X form in the same, Zn-containing (001) plane (such that the Cu_X antisites are nearest cation neighbors with Y_X but not each other), as this is the lowest-energy configuration for CZTS, CZTGS, CZGS, and CZGSSe; and (4) for $2Cu_{Cd}+Ge_{Cd}$ in wurtzite CCdGSSe, we increased threshold distance from 6 Å to 6.5 Å.

Defect	Protocol
V_{Cu}	Generate all symmetry-unique defect configurations
Cu_X+X_{Cu}	Generate all symmetry-unique defect configurations such that the distance between Cu_X and X_{Cu} < 4.5 Å
$2Cu_X+Y_X$	Generate all symmetry-unique defect configurations such that the distance between at least two of the three antisites < 6 Å

S6. ICSD Bulk Structures

Compositions, space groups, and ICSD collection codes for elements, binaries, ternaries, and quaternaries containing Cu, Zn, Cd, Sn, and S can be found in Table S2 of the Supporting Information for Ref. 12. Compositions and space groups for compounds containing Cu, Zn, Sn, Ge, S, and Se can be found in Table S4 of the Supplemental Material for Ref. 13.

Table S7. Compositions, space groups (and their number indices), ICSD collection codes, and DFT-SCAN polymorph energy differences (ΔE) for compounds containing Cu, Zn, Mg, Cd, Ge, Si, S, and Se that cannot be found in the supplementary information for Refs. 12 or 13. A few compounds do not have ΔE listed for the following reasons: Mg, Si, and SiS_2 have only one polymorph at ambient conditions in the ICSD; MgS, $ZnSe_2$, $CdSe_2$, Cd_4GeS_6, and Cd_4GeSe_6 have only one polymorph in the ICSD; and CuSe and Cu_8GeSe_6 have only one ordered polymorph in the ICSD.

Composition	Space Group (Number)	ICSD Collection Code	ΔE (eV/f.u.)
Elements			
Mg	$P6_3/mmc$ (194)	52260	
Si	$Fd\bar{3}mS$ (227)	51688	
Binaries			
MgS	$Fm\bar{3}m$ (225)	41234	
SiS_2	$Ibam$ (72)	27205	
Cu_2Se	$Fm\bar{3}m$ (225)	41140	0.000
	$F\bar{4}3m$ (216)	30230	0.067
CuSe	$P6_3/mmc$ (194)	82331	
$CuSe_2$	$Pnnm$ (58)	242	0.000
	$Pa\bar{3}$ (205)	243	0.022
ZnSe	$F\bar{4}3m$ (216)	77091	0.000
	$P6_3mc$ (186)	43595	0.010
$ZnSe_2$	$Pa\bar{3}$ (205)	652213	
CdSe	$P6_3mc$ (186)	415784	0.000
	$F\bar{4}3m$ (216)	41528	0.000
	$Fm\bar{3}m$ (225)	52833	0.225
$CdSe_2$	$Pa\bar{3}$ (205)	620416	
Ternaries			
Cu_2GeSe_3	$Imm2$ (44)	160386	0.000
	$C1c1$ (9)	192171	0.008
Cu_8GeSe_6	$P6_3cm$ (185)	69593	
Cd_4GeS_6	$C1c1$ (9)	26214	
Cd_4GeSe_6	$C1c1$ (9)	87087	

S7. Stability of Individual Point Defects vs. Clusters

Table S8. DFT-SCAN formation energies under Cu-poor conditions of individual, neutral point defects (Cu_X, X_{Cu}, and Y_X where X and Y are the divalent and tetravalent elements, respectively) and charge-compensated defect clusters (Cu_X+X_{Cu} and $2Cu_X+Y_X$) for CZTS (X = Zn, Y = Sn), CZGS (X = Zn, Y = Ge), and CCdGSSe (X = Cd, Y = Ge). "Cluster – ∑Separate" is the stabilization of the cluster vs. the separate point defects. For all defects, the neutral, charge-compensated defect cluster is more stable than the sum of the individual neutral point defects.

Material	X	Y	Formation energy (eV)					Cluster – ∑Separate (eV)	
			Cu_X	X_{Cu}	Y_X	Cu_X+X_{Cu}	$2Cu_X+Y_X$	Cu_X+X_{Cu}	$2Cu_X+Y_X$
CZTS	Zn	Sn	-0.20	1.34	1.85	0.22	0.67	-0.92	-0.78
CZGS	Zn	Ge	-0.19	1.51	2.00	0.15	0.92	-1.18	-0.71
CCdGSSe	Cd	Ge	0.02	1.49	1.57	0.38	1.51	-1.12	-0.09

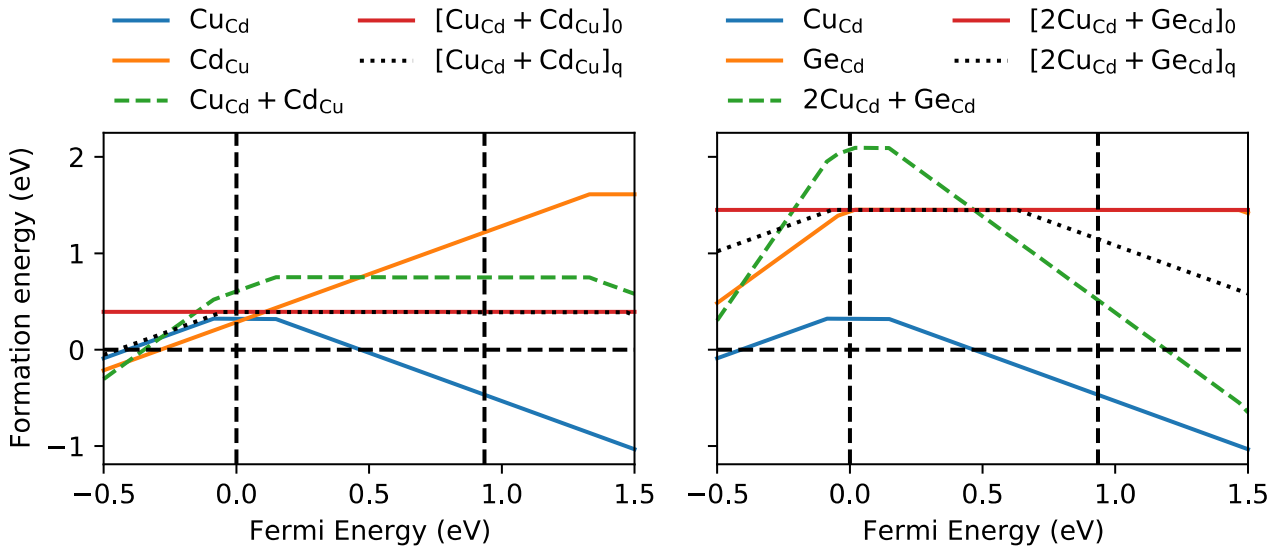

Figure S8. PBE+*U* formation energies under Cu-poor conditions of the CCdGSSe defects in Table S8 for different charge states (*q* = slope = 2, 1, 0, and -1). The left panel shows that the neutral $[Cu_{Cd}+Cd_{Cu}]_0$ cluster (solid red horizontal line) is more stable than the sum of the individual charged Cu_{Cd} and Cd_{Cu} antisites, i.e., "$Cu_{Cd}+Cd_{Cu}$" (dashed green line), and the neutral state is the most stable $[Cu_{Cd}+Cd_{Cu}]_q$ cluster charge state for all Fermi energies between the valence-band maximum (Fermi energy = 0 eV) and conduction-band minimum (Fermi energy = PBE+*U* band gap = 0.93 eV). The right panel shows that the sum of the individual charged Cu_{Cd} and Ge_{Cd} antisites, "$2Cu_{Cd}+Ge_{Cd}$" (dashed green line), is less stable than the neutral $[2Cu_{Cd}+Ge_{Cd}]_0$ cluster (solid red horizontal line) for Fermi energies from 0 to 0.47 eV and the neutral state is the most stable $[2Cu_{Cd}+Ge_{Cd}]_q$ cluster charge state for Fermi energies from 0 to 0.63 eV, i.e., where the equilibrium Fermi energy lies for p-doped CCdGSSe.

S8. Chemical Potential Limits for CZGSSe and CCdGSSe

Table S9. Referenced (i.e., referenced to the energies of pure elements in their ground-state structures) DFT-SCAN chemical potentials ($\mu^{ref.}$) under Cu-poor conditions for CZGSSe and CCdGSSe. The Cu-poor conditions are defined on page 5 of the main text. Note that here we have subtracted 0.27 eV/Ge from μ_{Ge} in accordance with the Ge correction described in reference 24.

Compounds in equilibrium	$\mu^{ref.}$ (eV/atom)					
	Cu	Zn	Cd	Ge	S	Se
Cu_2ZnGeS_4-ZnS-GeS_2-S-Se	-0.67	-1.88	n/a	-1.37	0.00	0.00
Cu_2CdGeS_4-Cd_4GeS_6-GeS_2-S-Se	-0.66	n/a	-1.52	-1.37	0.00	0.00

S9. Lowest Energy Defect Configurations

S9.1. Ge-substituted CZTS

S9.1.1. ↓CZTGS

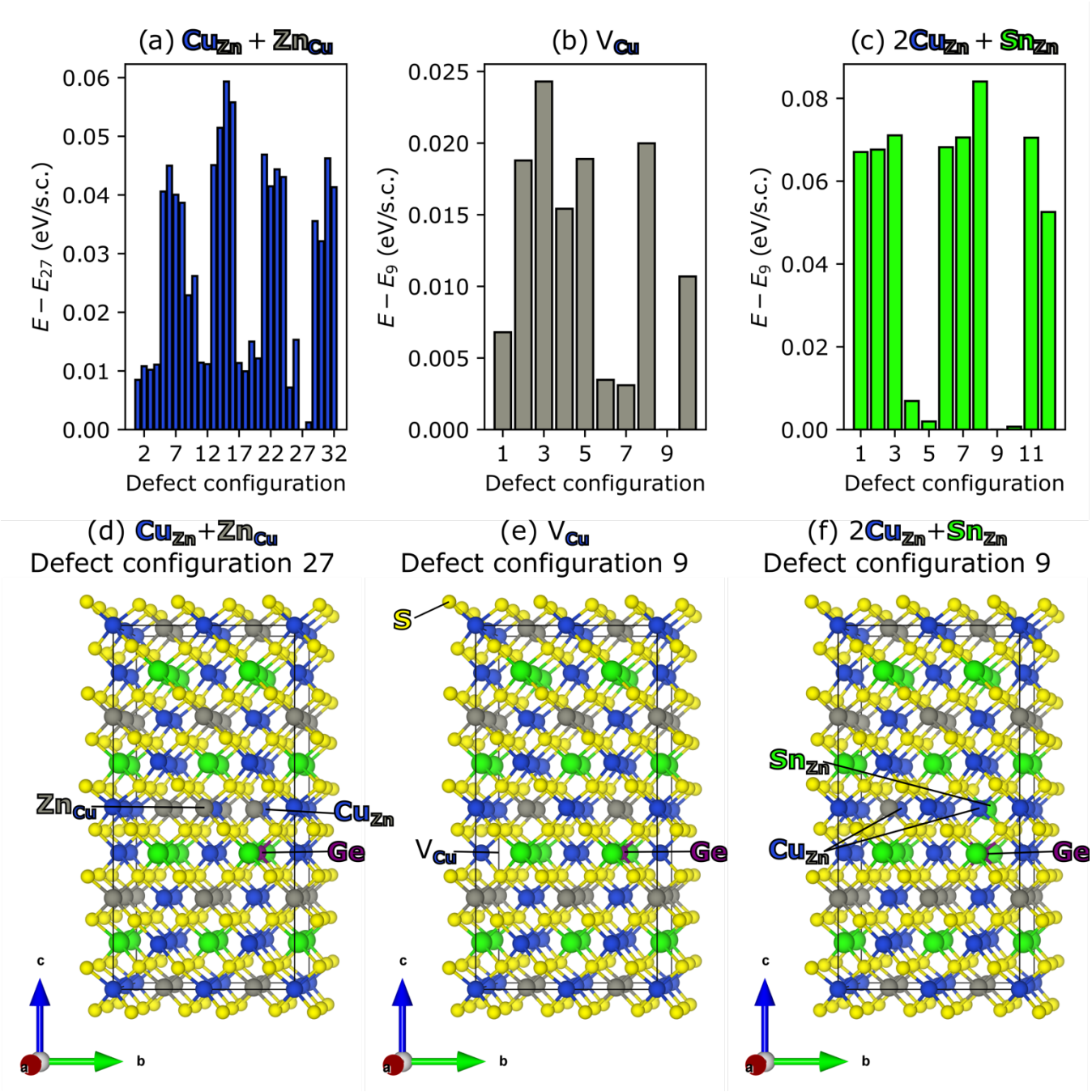

Figure S9. Relative energies of all symmetry-unique (a) Cu_{Zn}+Zn_{Cu}, (b) V_{Cu}, and (c) $2Cu_{Zn}$+Sn_{Zn} configurations in the 128-atom, $2 \times 2 \times 2$ supercell (s.c.) of kesterite ↓CZTGS. For Cu_{Zn}+Zn_{Cu}, V_{Cu}, and $2Cu_{Zn}$+Sn_{Zn}, energies are relative to configuration 27 (panel d), 9 (panel e), and 9 (panel f), respectively. Blue, gray, green, purple, and yellow balls correspond to Cu, Zn, Sn, Ge, and S, respectively (see multicolor labels). VASP POSCAR files containing the total energies, lattice geometries, and ionic positions of these structures can be found in "Structures/S9.1.1/".

S9.1.2. ↑CZTGS

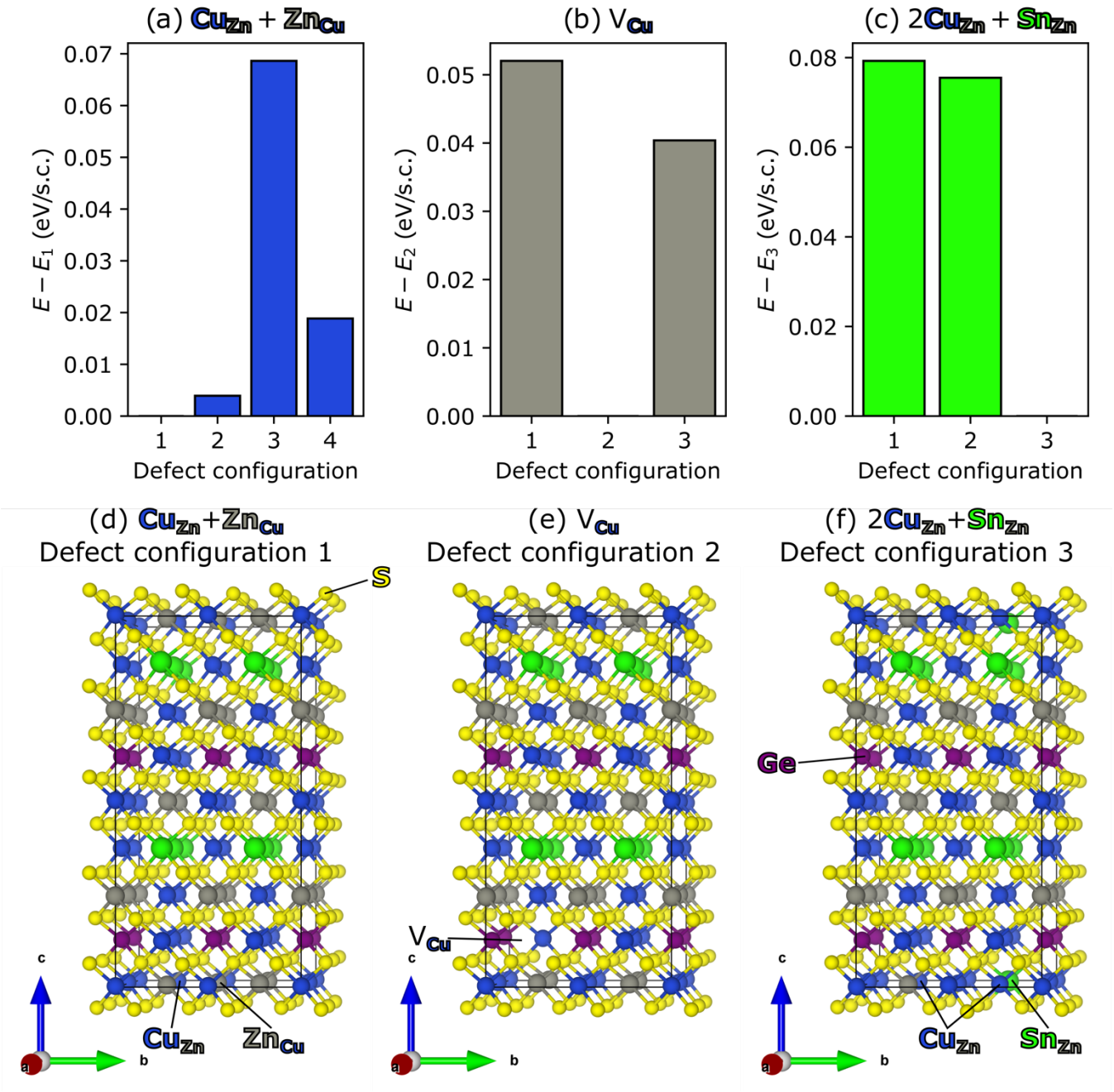

Figure S10. Relative energies of all symmetry-unique (a) Cu_{Zn}+Zn_{Cu}, (b) V_{Cu}, and (c) $2Cu_{Zn}$+Sn_{Zn} configurations in the 128-atom, $2 \times 2 \times 2$ supercell of kesterite ↑CZTGS. For Cu_{Zn}+Zn_{Cu}, V_{Cu}, and $2Cu_{Zn}$+Sn_{Zn}, energies are relative to configuration 1 (panel d), 2 (panel e), and 3 (panel f), respectively. Blue, gray, green, purple, and yellow balls correspond to Cu, Zn, Sn, Ge, and S, respectively (see multicolor labels). VASP POSCAR files containing the total energies, lattice geometries, and ionic positions of these structures can be found in "Structures/S9.1.2/".

S9.1.3. CZGS

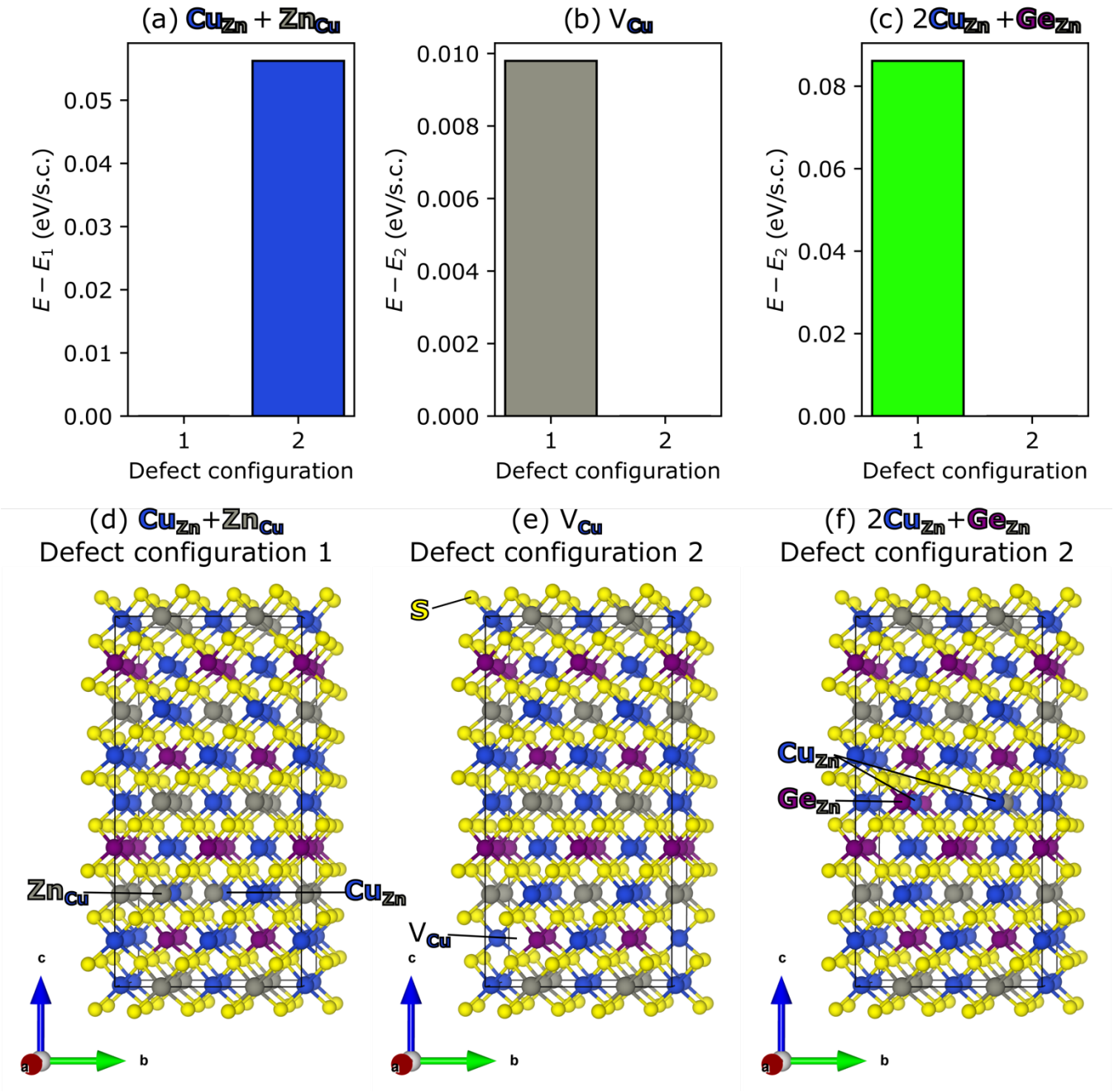

Figure S11. Relative energies of all symmetry-unique (a) Cu_{Zn}+Zn_{Cu}, (b) V_{Cu}, and (c) $2Cu_{Zn}$+Ge_{Zn} configurations in the 128-atom, $2 \times 2 \times 2$ supercell of kesterite CZGS. For Cu_{Zn}+Zn_{Cu}, V_{Cu}, and $2Cu_{Zn}$+Ge_{Zn}, energies are relative to configuration 1 (panel d), 2 (panel e), and 2 (panel f), respectively. Blue, gray, purple, and yellow balls correspond to Cu, Zn, Ge, and S, respectively (see multicolor labels). VASP POSCAR files containing the total energies, lattice geometries, and ionic positions of these structures can be found in "Structures/S9.1.3/".

S9.2. Se-substituted CZGS

S9.2.1. CZGSSe

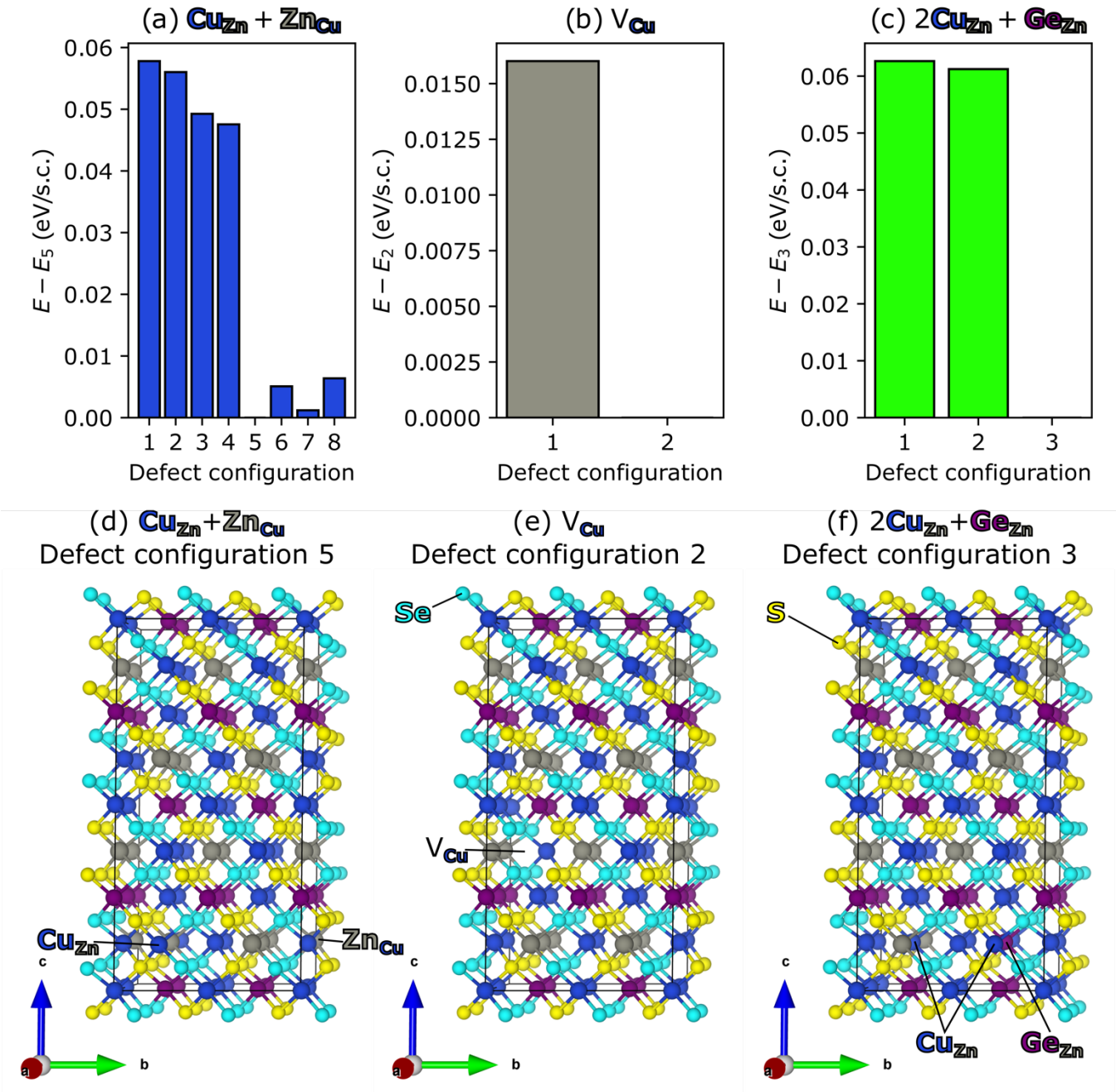

Figure S12. Relative energies of all symmetry-unique (a) Cu_{Zn}+Zn_{Cu}, (b) V_{Cu}, and (c) $2Cu_{Zn}$+Ge_{Zn} configurations in the 128-atom, $2 \times 2 \times 2$ supercell of kesterite CZGSSe. For Cu_{Zn}+Zn_{Cu}, V_{Cu}, and $2Cu_{Zn}$+Ge_{Zn}, energies are relative to configuration 5 (panel d), 2 (panel e), and 3 (panel f), respectively. Blue, gray, purple, yellow, and cyan balls correspond to Cu, Zn, Ge, S, and Se, respectively (see multicolor labels). VASP POSCAR files containing the total energies, lattice geometries, and ionic positions of these structures can be found in "Structures/S9.2.1/".

S9.2.2. CZGSe

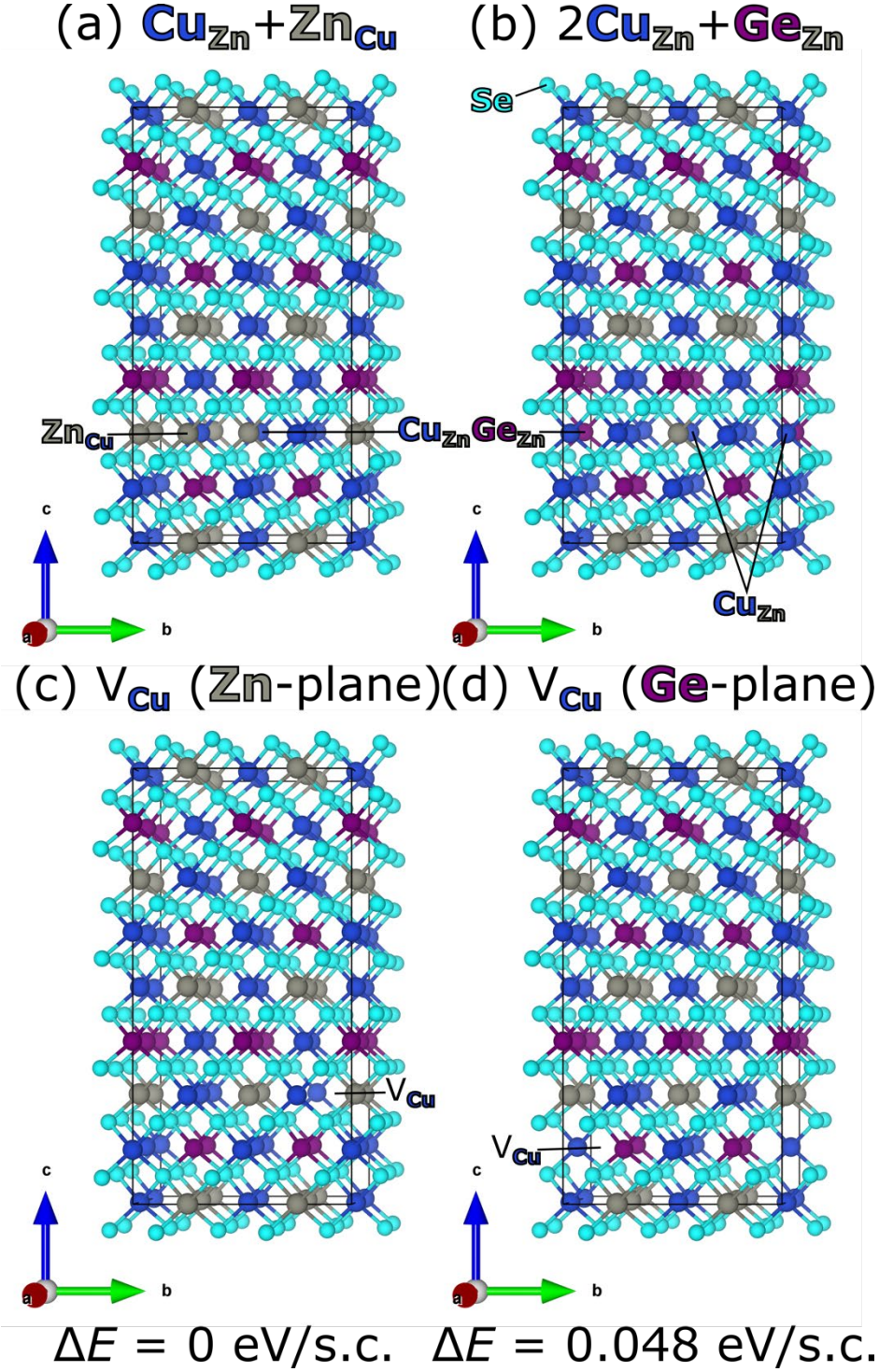

Figure S13. Ionic configuration of (a) Cu_{Zn}+Zn_{Cu}, (b) 2Cu_{Zn}+Ge_{Zn}, and V_{Cu} in both the (c) Zn- and (d) Ge-plane in the 128-atom, 2 × 2 × 2 supercell of kesterite CZGSe. V_{Cu} in the Ge-plane is 0.048 eV/s.c. less stable than that in the Zn-plane. Blue, gray, purple, and cyan balls correspond to Cu, Zn, Ge, and Se, respectively (see multicolor labels). VASP POSCAR files containing the total energies, lattice geometries, and ionic positions of these structures can be found in "Structures/S9.2.2/".

S9.3. Cd- and Se-substituted CZGS

S9.3.1. Stannite CCdGSSe

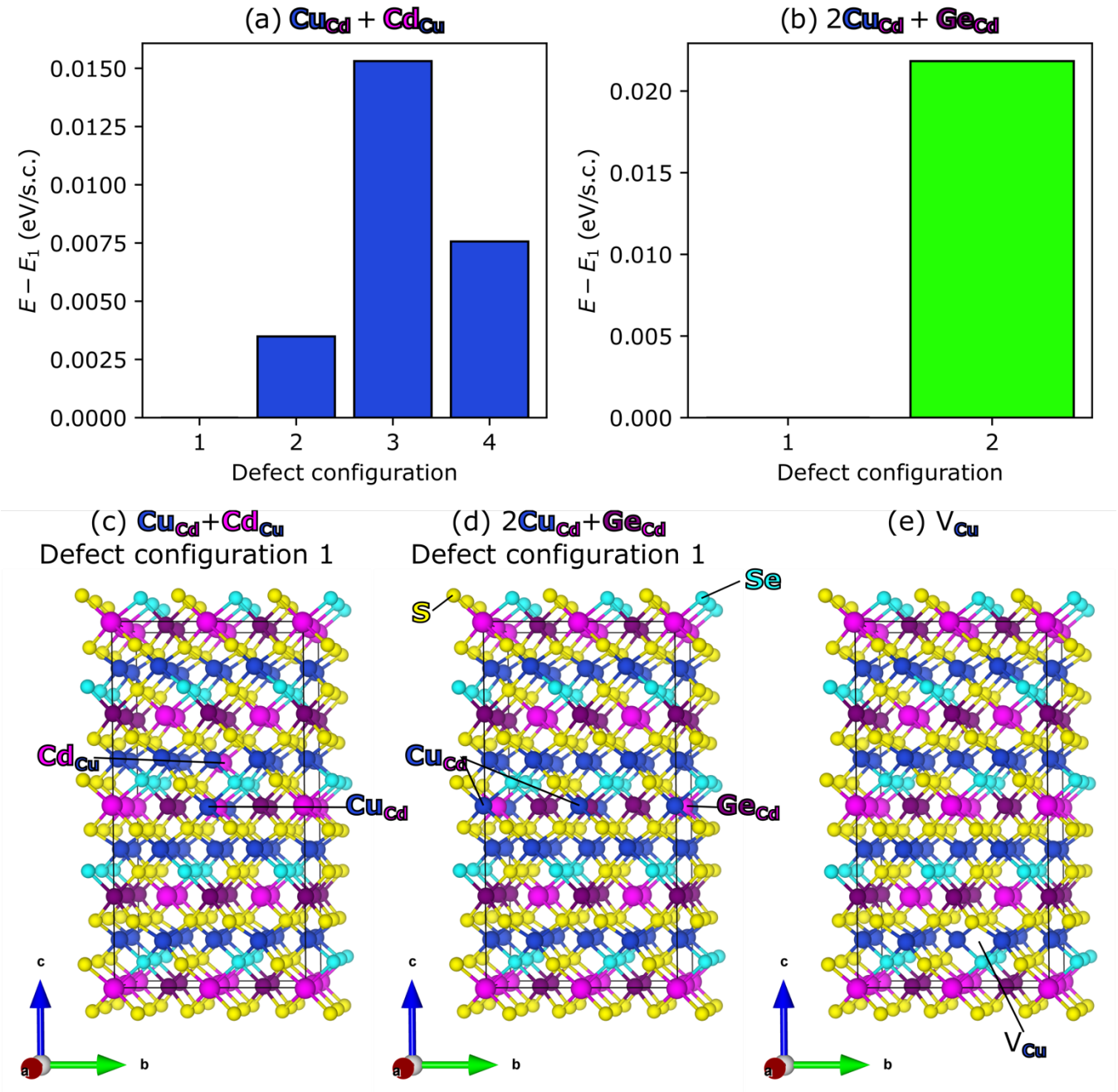

Figure S14. Relative energies of all symmetry-unique (a) Cu_{Cd}+Cd_{Cu} and (b) 2Cu_{Cd}+Ge_{Cd} configurations in the 128-atom, $2 \times 2 \times 2$ supercell of stannite CCdGSSe. For Cu_{Cd}+Cd_{Cu} and 2Cu_{Cd}+Ge_{Cd}, energies are relative to configuration 1 (panel c) and 1 (panel d), respectively. (e) Ionic configuration of V_{Cu}. Blue, magenta, purple, yellow, and cyan balls correspond to Cu, Cd, Ge, S, and Se, respectively (see multicolor labels). VASP POSCAR files containing the total energies, lattice geometries, and ionic positions of these structures can be found in "Structures/S9.3.1/".

S9.3.2. Wurtzite CCdGSSe

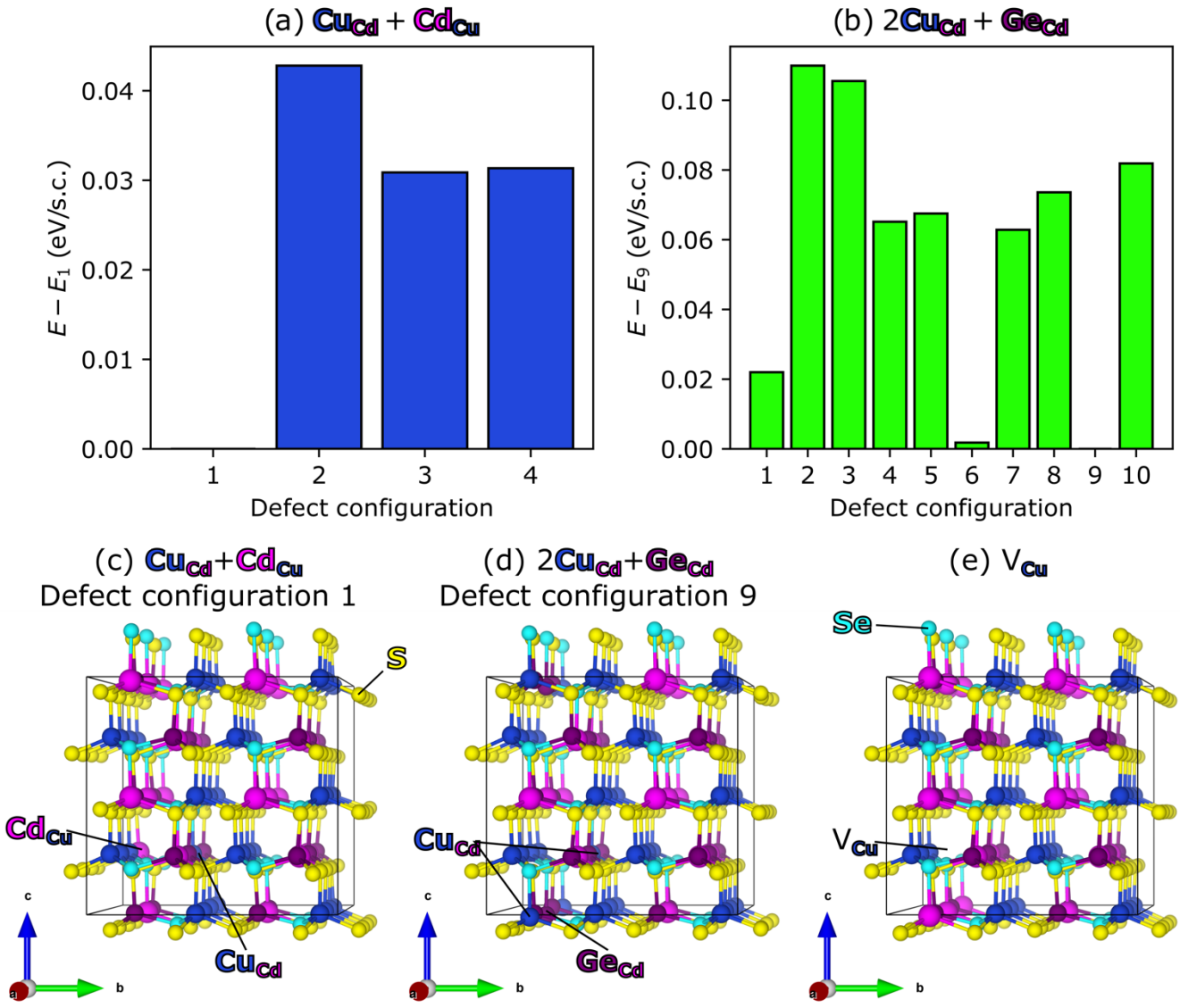

Figure S15. Relative energies of all symmetry-unique (a) Cu_{Cd}+Cd_{Cu} and (b) $2Cu_{Cd}$+Ge_{Cd} configurations in the 128-atom, $2 \times 2 \times 2$ supercell of wurtzite CCdGSSe. For Cu_{Cd}+Cd_{Cu} and $2Cu_{Cd}$+Ge_{Cd}, energies are relative to configuration 1 (panel c) and 9 (panel d), respectively. (e) Ionic configuration of V_{Cu}. Blue, magenta, purple, yellow, and cyan balls correspond to Cu, Cd, Ge, S, and Se, respectively (see multicolor labels). VASP POSCAR files containing the total energies, lattice geometries, and ionic positions of these structures can be found in "Structures/S9.3.2/".

S10. Effect of Cd- and Se-substitution on the Concentration of SRH Recombination Centers in CZGS

The decrease (x) in the concentration of $2Cu_X+Y_X$ SRH recombination centers in CZGS upon Cd- and Se-substitution is roughly given by

$$x = \frac{\exp\left(-\Delta E_f^d[CCdGSSe]/k_B T\right)}{\exp\left(-\Delta E_f^d[CZTS]/k_B T\right)} \quad \text{(S1)}$$

where $\Delta E_f^d[CCdGSSe] = 1.51$ eV is the formation energy of $2Cu_{Cd}+Ge_{Cd}$ in CCdGSSe, $\Delta E_f^d[CZTS] = 0.67$ eV is the formation energy of $2Cu_{Zn}+Sn_{Zn}$ in CZTS, k_B is the Boltzmann constant, and $T = 600$ K is the employed during selenization.[14,15] Inserting these values into equation (S1), we obtain $x = 8.8 \times 10^{-8}$.

S11. Influence of Anion Order in CCdGSSe on $Cu_{Cd}+Cd_{Cu}$ Formation Energies

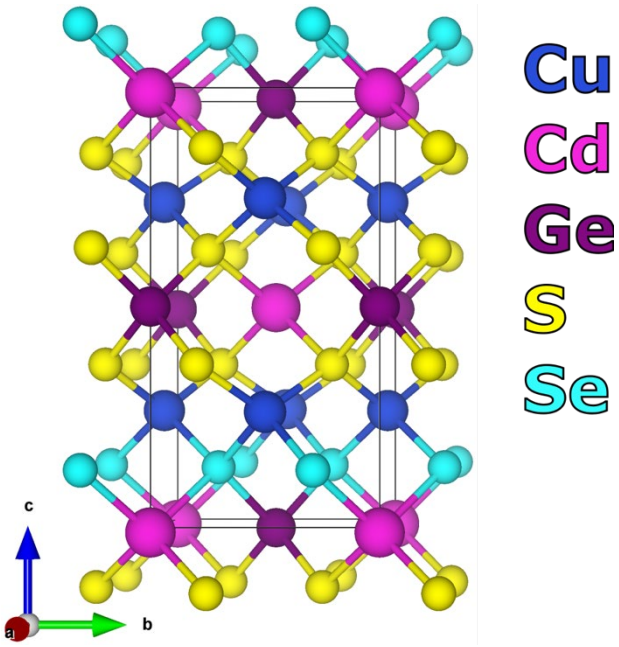

Figure S16. Crystal structure of the maximum-energy and maximally segregated anionic configuration of the stannite polymorph of CCdGSSe [ionic configuration 1 in Figure S7(a)].

Table S10. DFT-SCAN formation energies under Cu-poor conditions of all symmetry-unique Cu_{Cd}+Cd_{Cu} configurations in an S-Se disordered environment [each cation is exactly bonded to 1 Se atom, see ionic configuration 4 in Figure S7(a)] and S/Se-rich environments [cations have either 0 or 2 Se-bonds, see ionic configuration 1 in Figure S7(a)] CCdGSSe. Figures 6(a) in the main text and S16 show the crystal structures of S-Se disordered and S-Se segregated stannite CCdGSSe, respectively. Blue, magenta, purple, yellow, and cyan balls correspond to Cu, Cd, Ge, S, and Se, respectively.

Ionic configuration	Defect configuration	ΔE_f^d (eV)
4	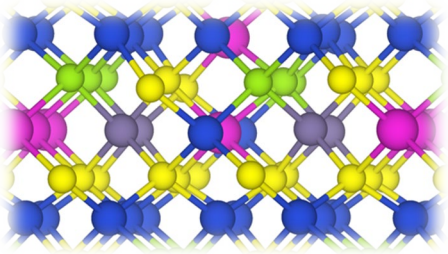	0.40
4	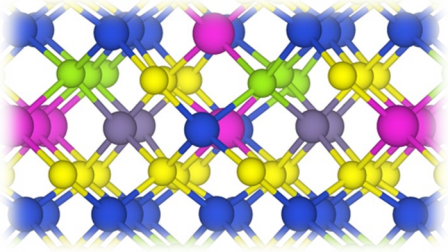	0.39
4	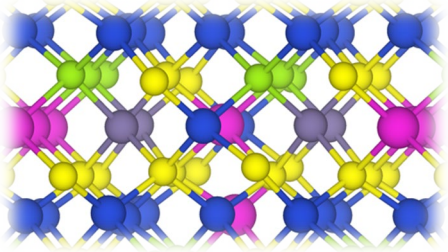	0.38
4	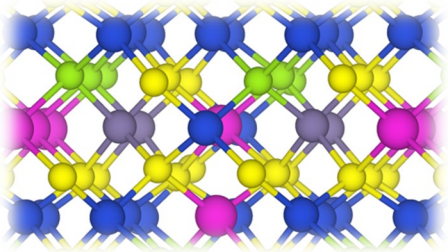	0.39
1	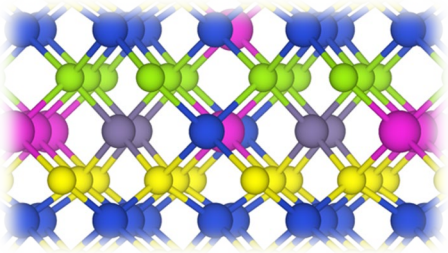	0.29

1	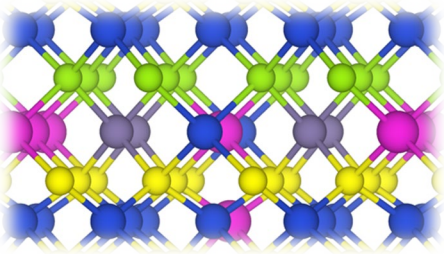	0.33
1	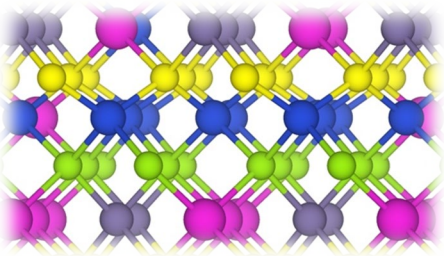	0.26
1	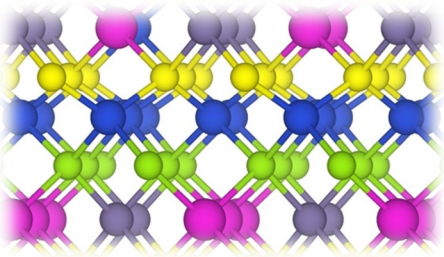	0.29

S12. Intrinsic Stability/Instability of CZTS, CZGS, CZGSSe, and CCdGSSe

Table S11. DFT-SCAN energy above the hull (E_{hull}) for CZTS, CZGS, CZGSSe, and CCdGSSe.

Compound	E_{hull} (eV/atom)
CZTS	0.000
CZGS	0.000
CZGSSe	0.073
CCdGSSe	0.005

S13. Experimental Band Gaps of Cu_2CdGeS_4 and $Cu_2CdGeSe_4$ and Predicted Defect Formation Energies for Cu_2CdGeS_3Se and $Cu_2CdGeS_2Se_2$

Table S12. Experimental band gaps of Cu_2CdGeS_4 and $Cu_2CdGeSe_4$. PL is photoluminescence and EQE is external quantum efficiency.

Compound	Band gap (eV)	Method	Reference
Cu_2CdGeS_4	2.05	UV-Vis absorption	16
Cu_2CdGeS_4	2.05	UV-Vis absorption	17
Cu_2CdGeS_4	1.85	UV-Vis absorption	18
Cu_2CdGeS_4	1.97	Micro- PL	19
$Cu_2CdGeSe_4$	1.20	UV-Vis absorption	20
$Cu_2CdGeSe_4$	1.20	UV-Vis absorption	21
$Cu_2CdGeSe_4$	1.14-1.27	EQE	22
$Cu_2CdGeSe_4$	1.223-1.257	Reflectivity	23

Table S13. DFT-SCAN defect formation energies (ΔE_f^d) for Cu_2CdGeS_3Se and $Cu_2CdGeS_2Se_2$ under Cu-poor conditions.

Compound	Defect formation energy (eV)		
	$Cu_{Cd}+Cd_{Cu}$	V_{Cu}	$2Cu_{Cd}+Ge_{Cd}$
Cu_2CdGeS_3Se	0.38	-0.04	1.51
$Cu_2CdGeS_2Se_2$	0.30	-0.19	1.45

S14. Formation Energy of Anion Vacancies in CCdGSSe

Table S14. DFT-SCAN formation energies of V_S and V_S+Cu_X in kesterite CZTS, kesterite CZGS, stannite CCdTS, stannite CCdGS, and stannite CCdGSSe, and V_{Se} and V_{Se}+Cu_{Cd} in stannite CCdGSSe under Cu-poor conditions (i.e., when CCdGS, Cd_4GeS_6, GeS_2, S, and Se are in equilibrium). X is Zn or Cd.

Material	X (2+ site)	4+ site	Formation energy (eV)			
			V_S	V_S+Cu_X	V_{Se}	V_{Se}+Cu_X
CZTS	Zn	Sn	1.96	1.67	n/a	n/a
CZGS	Zn	Ge	2.30	1.76	n/a	n/a
CCdTS	Cd	Sn	1.64	1.32	n/a	n/a
CCdGS	Cd	Ge	2.01	1.85	n/a	n/a
CCdGSSe	Cd	Ge	2.00	1.98	1.85	1.66

References

(1) Zhong, G.; Tse, K.; Zhang, Y.; Li, X.; Huang, L.; Yang, C.; Zhu, J.; Zeng, Z.; Zhang, Z.; Xiao, X. Induced Effects by the Substitution of Zn in Cu_2ZnSnX_4 (X= S and Se). *Thin Solid Films* **2016**, *603*, 224–229. https://doi.org/10.1016/j.tsf.2016.02.005.

(2) Kubaschewski, O.; Alcock, C. B. *Metallurgical Thermochemistry*, 5th ed.; Raynor, G. V., Ed.; Pergamon Press, 1959; Vol. 12. https://doi.org/10.1063/1.3060816.

(3) Takéuchi, Y.; Sasaki, S.; Bente, K. A.; Tsukimura, K. Electron Density Distribution in MgS. *Acta Crystallogr. Sect. B Struct. Sci.* **1993**, *49* (4), 780–781. https://doi.org/10.1107/S0108768192013521.

(4) Peters, J.; Krebs, B. Silicon Disulphide and Silicon Diselenide: A Reinvestigation. *Acta Crystallogr. Sect. B Struct. Crystallogr. Cryst. Chem.* **1982**, *38* (4), 1270–1272. https://doi.org/10.1107/S0567740882005469.

(5) Otte, H. M. Lattice Parameter Determinations with an X-Ray Spectrogoniometer by the Debye-Scherrer Method and the Effect of Specimen Condition. *J. Appl. Phys.* **1961**, *32* (8), 1536–1546. https://doi.org/10.1063/1.1728392.

(6) Nuss, J.; Wedig, U.; Kirfel, A.; Jansen, M. The Structural Anomaly of Zinc: Evolution of Lattice Constants and Parameters of Thermal Motion in the Temperature Range of 40 to 500 K. *Zeitschrift für Anorg. und Allg. Chemie* **2010**, *636* (2), 309–313. https://doi.org/10.1002/zaac.200900460.

(7) Hull, A. W. A New Method of X-Ray Crystal Analysis. *Phys. Rev.* **1917**, *10* (6), 661–696. https://doi.org/10.1103/PhysRev.10.661.

(8) Thewlis, J.; Davey, A. R. Thermal Expansion of Grey Tin. *Nature* **1954**, *174* (4439), 1011–1011. https://doi.org/10.1038/1741011a0.

(9) Többens, D. M.; Stüßer, N.; Knorr, K.; Mayer, H. M.; Lampert, G. E9: The New High-Resolution Neutron Powder Diffractometer at the Berlin Neutron Scattering Center. *Mater. Sci. Forum* **2001**, *378–381* (I), 288–293. https://doi.org/10.4028/www.scientific.net/MSF.378-381.288.

(10) Pawley, G. S.; Rinaldi, R. P. Constrained Refinement of Orthorhombic Sulphur. *Acta Crystallogr. Sect. B*

Struct. Crystallogr. Cryst. Chem. **1972**, *28* (12), 3605–3609. https://doi.org/10.1107/S0567740872008428.

(11) Levcenco, S.; Dumcenco, D.; Huang, Y. S.; Arushanov, E.; Tezlevan, V.; Tiong, K. K.; Du, C. H. Near Band Edge Anisotropic Optical Transitions in Wide Band Gap Semiconductor Cu_2ZnSiS_4. *J. Appl. Phys.* **2010**, *108* (7), 073508. https://doi.org/10.1063/1.3490219.

(12) Sai Gautam, G.; Senftle, T. P.; Carter, E. A. Understanding the Effects of Cd and Ag Doping in Cu_2ZnSnS_4 Solar Cells. *Chem. Mater.* **2018**, *30* (14), 4543–4555. https://doi.org/10.1021/acs.chemmater.8b00677.

(13) Wexler, R. B.; Sai Gautam, G.; Carter, E. A. Exchange-Correlation Functional Challenges in Modeling Quaternary Chalcogenides. *Submitted*.

(14) Redinger, A.; Berg, D. M.; Dale, P. J.; Siebentritt, S. The Consequences of Kesterite Equilibria for Efficient Solar Cells. *J. Am. Chem. Soc.* **2011**, *133* (10), 3320–3323. https://doi.org/10.1021/ja111713g.

(15) Wang, G.; Zhao, W.; Cui, Y.; Tian, Q.; Gao, S.; Huang, L.; Pan, D. Fabrication of a $Cu_2ZnSn(S,Se)_4$ Photovoltaic Device by a Low-Toxicity Ethanol Solution Process. *ACS Appl. Mater. Interfaces* **2013**, *5* (20), 10042–10047. https://doi.org/10.1021/am402558a.

(16) Davydyuk, G. Y.; Parasyuk, O. V.; Romanyuk, Y. E.; Semenyuk, S. A.; Zaremba, V. I.; Piskach, L. V.; Kozioł, J. J.; Halka, V. O. Single Crystal Growth and Physical Properties of the Cu_2CdGeS_4 Compound. *J. Alloys Compd.* **2002**, *339* (1–2), 40–45. https://doi.org/10.1016/S0925-8388(01)01987-9.

(17) Davidyuk, G. E.; Parasyuk, O. V.; Semenyuk, S. A.; Romanyuk, Y. E. Electrical and Optical Properties of Cu_2CdGeS_4 Single Crystals. *Inorg. Mater.* **2003**, *39* (9), 919–923. https://doi.org/https://doi.org/10.1023/A:1025596903080.

(18) Brik, M. G.; Kityk, I. V.; Parasyuk, O. V.; Myronchuk, G. L. Photoinduced Features of Energy Bandgap in Quaternary Cu_2CdGeS_4 Crystals. *J. Phys. Condens. Matter* **2013**, *25* (50), 505802. https://doi.org/10.1088/0953-8984/25/50/505802.

(19) Krustok, J.; Raadik, T.; Li, X.; Kauk-Kuusik, M.; Timmo, K.; Oueslati, S.; Grossberg, M. Study of Point Defects in Wide-Bandgap Cu_2CdGeS_4 Microcrystals by Temperature and Laser Power Dependent Photoluminescence Spectroscopy. *J. Phys. D. Appl. Phys.* **2020**, *53* (27), 275102. https://doi.org/10.1088/1361-6463/ab83c1.

(20) Matsushita, H.; Ichikawa, T.; Katsui, A. Structural, Thermodynamical and Optical Properties of Cu_2-II-IV-VI_4 Quaternary Compounds. *J. Mater. Sci.* **2005**, *40* (8), 2003–2005. https://doi.org/10.1007/s10853-005-1223-5.

(21) Matsushita, H.; Maeda, T.; Katsui, A.; Takizawa, T. Thermal Analysis and Synthesis from the Melts of Cu-Based Quaternary Compounds Cu–III–IV–VI_4 and Cu_2–II–IV–VI_4 (II=Zn,Cd; III=Ga,In; IV=Ge,Sn; VI=Se). *J. Cryst. Growth* **2000**, *208* (1–4), 416–422. https://doi.org/10.1016/S0022-0248(99)00468-6.

(22) Kauk-Kuusik, M.; Li, X.; Pilvet, M.; Timmo, K.; Grossberg, M.; Raadik, T.; Danilson, M.; Mikli, V.; Altosaar, M.; Krustok, J.; Raudoja, J. Study of $Cu_2CdGeSe_4$ Monograin Powders Synthesized by Molten Salt Method for Photovoltaic Applications. *Thin Solid Films* **2018**, *666* (September), 15–19. https://doi.org/10.1016/j.tsf.2018.09.025.

(23) Krustok, J.; Raadik, T.; Kaupmees, R.; Grossberg, M.; Kauk-Kuusik, M.; Timmo, K.; Mere, A. Observation of Band Gap Fluctuations and Carrier Localization in $Cu_2CdGeSe_4$. *J. Phys. D. Appl. Phys.* **2019**, *52* (28), 285102. https://doi.org/10.1088/1361-6463/ab1afd.

(24) Wexler, R. B.; Sai Gautam, G.; Carter, E. A. Exchange-correlation functional challenges in modeling quaternary chalcogenides. *Phys. Rev. B* **2020**, *102* (5), 054101. https://doi.org/10.1103/PhysRevB.102.054101.

(25) Togo, A.; Tanaka, I. First Principles Phonon Calculations in Materials Science. *Scr. Mater.* **2015**, *108*, 1–5. https://doi.org/10.1016/j.scriptamat.2015.07.021.

(26) Alverdiev, I. J.; Abbasova, V. A.; Yusibov, Y. A.; Tagiev, D. B.; Babanly, M. B. Thermodynamic Study of Cu_2GeS_3 and $Cu_{2-x}Ag_xGeS_3$ Solid Solutions by the EMF Method with a $Cu_4RbCl_3I_2$ Solid Electrolyte. *Russ. J. Electrochem.* **2018**, *54* (2), 195–200. https://doi.org/10.1134/S1023193518020027.